# Adaptive Observer for Dynamic Voltage Restorer with Optimized Proportional Integral Gains*

*Sabha Raj Arya*[1*], *Rakesh Maurya*[1], *Talada Appala Naidu*[1] *and Baladhandautham Chitti Babu*[2]
(1. Department of Electrical Engineering, Sardar Vallabhbhai National Institute of Technology, Surat 395007, India;
2. Department of Electronics and Communication Engineering, IIITDM, Chennai 600127, India)

**Abstract**: An algorithm based on a sliding-mode adaptive observer is proposed for the effective control of dynamic voltage restorers (DVRs). Three single-phase voltage source converter-based topologies are implemented for the DVR. In this control, frequency adaption is considered for estimating the phase angle, system frequency, and fundamental component of the disturbed input voltage signals. The estimated fundamental component of the supply voltage is used to generate the DVR reference load voltage. The phase jump in the supply voltage is also considered for DVR compensation studies along with voltage sag, swell, and voltage distortions. For this purpose, the gains of the proportional integral (PI) controllers used in this control algorithm are estimated using a nature-inspired optimization approach for the desired response. A moth flame optimization algorithm is implemented for PI controller gain tuning owing to the advantage of finding the best solution by each moth's search and updating it. Through Matlab simulation and hardware testing, the performance of the DVR with an adaptive observer is found to be satisfactory for supply voltage sag, swell, phase jump, and voltage distortions.

**Keywords**: Adaptive observer, phase jump, power quality, frequency estimation, DVR, triangular wave

## 1 Introduction

The usage of power electronic devices has been drastically increasing in domestic and commercial sectors to meet the requirement of a desired response [1]. However, power electronics solve power quality (PQ) issues they raise themselves [2]. The PQ problems are based on the voltage and current, and depend on the source of the supply voltage and connected load, respectively [3]. The voltage-based PQ problems are voltage swell, voltage sag, imbalance, and harmonics in the voltage waveform. Initial solutions to the PQ issues were static voltage compensators, which later began to use active filters, owing to their dependency on passive components [4]. Patel et al. [5] analyzed the placement of a dynamic voltage restorer (DVR) on distribution system buses where the maximum voltage dip occurs. Mansoor et al. [6] reviewed the issues with DVRs in terms of cost, efficiency, reliability, and response time.

A DVR is a power quality improvement device, introduced for power quality owing to its interesting characteristics for resolving voltage-related issues [7-11]. Jindal et al. [7] studied load voltage control using a rectifier-supported DVR with zero cross-detector-based control. The author in Ref. [8] discussed a DVR with minimum power injection during sag mitigation by measuring the magnitude and phase angle of the compensated voltage. Ajaei et al. [9] presented a DVR for sag compensation with linear and nonlinear loads during different types of faults in the lines. In a medium-voltage distribution system for voltage dip compensation, DVRs have been studied with different types of rectifier connections [10]. Abdollahzadeh et al. [11] used symmetrical component estimation control for DVRs to compensate for the voltage sag. DVRs have been implemented with different types of control algorithms for voltage-related PQ improvement [12-18]. Leon et al. [12] presented a control strategy that is used to improve system stability in wind farms by separating the sequence components. The authors in Ref. [13] developed a control based on an elliptical compensation approach for DVRs to compensate for the voltage-related disturbances in the supply. A synchronous reference frame theory-based control was

Manuscript received June 20, 2021; revised November 12, 2021; accepted December 31, 2021. Date of publication March 31, 2022; date of current version January 21, 2022.
* Corresponding Author, E-mail: sabharaj79@gmail.com
* Supported by Science and Engineering Research Board-New Delhi, India, Project (Extra Mural Research Funding Scheme), Grant No. No.SB/S3/EECE/030/2016.
Digital Object Identifier: 10.23919/CJEE.2022.000004

adopted for DVR control in a fault ride through the application of wind turbines [14]. In Ref. [15], the authors described the DVR control system based on synchronous reference frame theory along with particle swarm optimization for gain estimation in the control. Chen et al. [16] proposed an SPLL control algorithm with a combination of the least error square (LES) to control the cascaded H-bridge DVR. The authors in Ref. [17] implanted a 4-wire DVR with a rectifier-supported configuration that uses an LES method with fixed or variable window lengths to improve the frequency response and reduce the computational burden. Fernandes et al. [18] proposed a repetitive control scheme that does not require any selective harmonic elimination filters that use recursive least squares to estimate the phase angle and amplitude.

The increased region of existence for single-phase DVRs was presented using sliding mode control (SMC) in Ref. [19], which compensated for disturbances in the supply voltage. The listed feature of SMC is a fast dynamic response without overshoots in the compensated voltage. Slotine et al. [20] designed a state observer using a sliding surface that provides advantages such as robustness to parametric indefiniteness and easy applicability to nonlinear systems. Based on the combined advantages of SMC and observer using a sliding surface, Ahmed et al. [21] proposed an adaptive observer-based sliding mode controller for the estimation of phase and frequency. Owing to the presence of low pass filters (LPFs) present in the PLL for accurate estimation of the phase and frequency of the input signal, it reduces the slowness. In addition to the above advantages, the sliding mode adaptive observer (SMAO)'s features, such as estimation of phase angle, frequency estimation, and fundamental component estimation, allow us to use it in the DVR control operation. Most control algorithms in power electronics applications use proportional integral (PI) controllers to achieve better control performance. The authors in Ref. [22] introduced an optimization method for the automatic tuning of PI controllers for temperature control. Using exact optimization methods for real-time problems is not efficient because of their intrinsic characteristics, such as multi-modality, high-dimensionality, parameter dependence, and non-differentiability. Thus, approximate methods have been used as solutions [23]. The several approximate methods—also called optimization approaches—have been classified with respect to their nature of inspiration, and then analyzed. A nature-inspired optimization algorithm called moth flame optimization (MFO) has been studied for real engineering problems in Ref. [24].

This paper describes the implementation of an SMAO-based control algorithm for a three-phase DVR along with automatic tuning of PI controller gains using the MFO algorithm. The SMAO has the ability to estimate the fundamental component and phase angle of the disturbed input signals. For the estimation of the system frequency, the SMAO uses the adaptation of its frequency. This improves the estimation performance of the control algorithm. The MFO algorithm is a nature-inspired optimization algorithm that is simple to implement; it mimics the characteristics of moths that use transverse orientation for traveling in the nighttime, which improves the speed of the solution. The DVR system with the proposed control is tested for voltage sag, swell, and distortions, as well as the phase shift in the supply voltage. Simulation and test results are presented in this paper to evaluate the robustness of the proposed control algorithm for DVRs. The results demonstrate that the DVR with an SMAO control algorithm with MFO-based tuning PI gains can compensate for the above-mentioned voltage-related PQ issues in the supply system.

## 2 Three phase DVR system configuration

A three-phase voltage source converter (VSC) is developed, and it is connected to a three-phase system through three single-phase injection transformers to create a complete DVR system. The three-phase ac grid is made non-ideal by connecting different loads on the same bus. To create a sag in the supply, a high inductive load is switched ON, whereas the capacitive load is switched ON to create a swell in the voltage. A non-linear load is connected at the same supply point to create distortions in the supply voltage. Similarly, a single load is connected between the two phases to create an imbalance. The sensitive or critical load to be protected is a resistive inductive (RL) linear load, which is to be maintained at a constant load voltage ($v_L$), as shown in Fig. 1. The non-ideal AC supply system

is connected to a sensitive load through injection transformers and a voltage source converter in the supply system. As proposed, the system configuration is self-supported, and the energy storage system is replaced by a capacitor ($C_{DC}$) that stores energy in it and supports the voltage dynamics in the supply voltage ($v_s$), whenever required. The interfacing inductors "$L_i$" are employed to minimize the ripples in the current waveform of the converter. The switching harmonics generated by the VSCs must be passed through filters ($R_f$ , $C_f$) before being injected into the line. The power devices used in the VSC are named as $s_{a1}$, $s_{a2}$, $s_{a3}$, and $s_{a4}$ for phase "a" , $s_{b1}$, $s_{b2}$, $s_{b3}$, and $s_{b4}$ for phase "b" , and $s_{c1}$, $s_{c2}$, $s_{c3}$, and $s_{c4}$ for phase "c". Based on the ratings of the load and supply voltage, the DVR system configuration can be made suitable for the compensation of listed issues in supply voltage with suitable selection of the transformation ratio and rating of the injection transformers. The system parameters selected for the simulation and test performance are given in Appendix-A and Appendix-B, respectively.

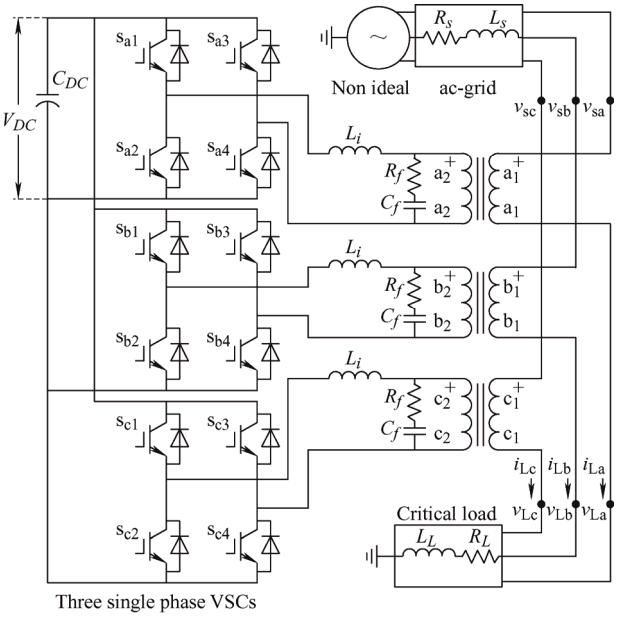


Fig. 1 Three single-phase voltage source converter (VSC) used as three phase dynamic voltage restorer (DVR)

## 3 Control algorithm

In any power electronics-based system, the accuracy and speed of the control directly affect the system performance. Therefore, an adaptive observer-based sliding mode controller is proposed for estimating the fundamental component for generating gate pulses to the VSC. In this control, frequency adaption is considered while estimating the phase angle ($\varphi$) of the input signal. Therefore, three single units of the adaptive observer are combined to estimate the three-phase fundamental components, ($v_{sf}$), out of the disturbed three-phase input supply voltages, ($v_s$). An optimization technique called MFO is used for the tuning of the PI controllers instead of trial and error tuning. This section includes the mathematical description of the SMAO-based control algorithm for the estimation of the fundamental component and phase angle ($\varphi$), PI controller gain estimation, three-phase load reference voltage ( $v_L^*$ ) generation, and gate pulse generation. Fig. 2 depicts the control circuit for the DVR, which includes the SMAO-based

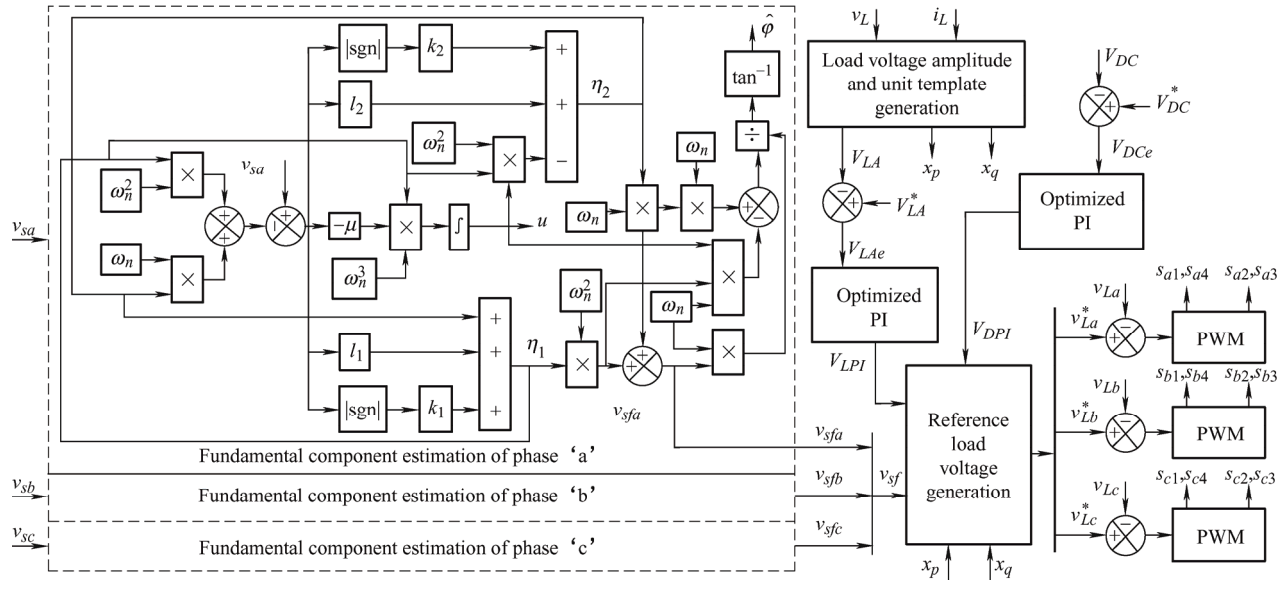


Fig. 2 Control circuit for DVR based on adaptive observer

fundamental extractor, reference load voltage generator, and PWM pulse generator. This section presents the control algorithm sub-section wise, along with the process of PI controller gain optimization.

### 3.1 Fundamental component and phase angle estimation using SMAO

A mathematical description of the SMAO is presented for phase "a", as phases "b" and "c" are analogous. Eq. (1) is considered as the disturbed input signal for which the fundamental component ($v_1$) and phase angle ($\varphi$) must be estimated.

$$\boldsymbol{v}_{sa} = A_m \sin(\omega t - \theta) = A_m \sin\varphi \tag{1}$$

where $A_m$ and $\omega$ are the magnitude of the input signal and the system frequency in radians, respectively. The state-space model of the input signal dynamics is set as Eqs. (2) and (3)

$$\boldsymbol{v} = \begin{bmatrix} v_1 \\ v_2 \end{bmatrix} = \begin{bmatrix} A_m \sin(\omega t - \theta) \\ A_m \omega \cos(\omega t - \theta) \end{bmatrix} \tag{2}$$

$$\begin{cases} \dot{v} = \begin{bmatrix} \dot{v}_1 \\ \dot{v}_2 \end{bmatrix} = \boldsymbol{P}\boldsymbol{v} \\ \boldsymbol{y} = \boldsymbol{Q}\boldsymbol{v} \end{cases} \tag{3}$$

where, $v_2 = \dot{v}_1$, $\dot{v}_2 = -u\omega_n^2 A_m \sin(\omega t - \theta)$, $\boldsymbol{P} = \begin{bmatrix} 0 & 1 \\ -u\omega_n^2 & 0 \end{bmatrix}$; $\boldsymbol{Q} = [1 \quad 0]$; assuming parameter $u = \dfrac{\omega^2}{\omega_n^2}$, where $\omega$ is system frequency and $\omega_n$ is the nominal system angular frequency. It must be understood that the estimation of $\omega_n$ can be attained by estimating $u$; otherwise, to find $\omega_n$, an adaptation of $u$ is necessary. Thus, its state transformation can be written as in Eq. (4). In $\eta$ system Eq. (3) can be modified as Eq. (5).

$$\boldsymbol{\eta} = \begin{bmatrix} \eta_1 \\ \eta_2 \end{bmatrix} = \boldsymbol{R} \times \boldsymbol{v} = \frac{1}{1+u} \begin{bmatrix} \dfrac{1}{\omega_n^2} & \dfrac{1}{\omega_n^3} \\ \dfrac{u}{\omega_n} & \dfrac{1}{\omega_n^2} \end{bmatrix} \times \begin{bmatrix} v_1 \\ v_2 \end{bmatrix} \tag{4}$$

$$\begin{cases} \dot{\boldsymbol{\eta}} = \boldsymbol{A}\boldsymbol{\eta} \\ \boldsymbol{y} = \boldsymbol{B}\boldsymbol{\eta} \end{cases} \tag{5}$$

where $\boldsymbol{A} = \boldsymbol{R}\boldsymbol{P}\boldsymbol{R}^{-1} = \boldsymbol{P}$; $\boldsymbol{B} = \boldsymbol{Q}\boldsymbol{R}^{-1} = [\omega_n^2 \quad \omega_n]$.

A sliding control methodology has been developed to attain accurate tracking for nonlinear time-varying multi-variable systems in the presence of disturbance and parameter variations [20-21]. The structure of the sliding mode observer for dynamic system Eq. (5) was designed and represented as Eq. (6)

$$\dot{\hat{\boldsymbol{\eta}}} = \hat{\boldsymbol{A}}\hat{\boldsymbol{\eta}} + \boldsymbol{\alpha} \times (\boldsymbol{y} - \boldsymbol{B}\boldsymbol{\eta}) + \boldsymbol{\beta} \times \mathrm{sgn}(\boldsymbol{y} - \boldsymbol{B}\boldsymbol{\eta}) \tag{6}$$

where $\boldsymbol{\alpha} = [\alpha_1 \quad \alpha_2]^{\mathrm{T}}$ and $\boldsymbol{\beta} = [\beta_1 \quad \beta_2]^{\mathrm{T}}$ are the observer gain matrices, which are selected after observing the performance. As observer Eq. (6) depends on the value of "$u$", there should be a requirement for some updating law to estimating it. It is considered that the output error of observer "$\boldsymbol{e}$" is as follows

$$\boldsymbol{e} = (\boldsymbol{y} - \boldsymbol{B}\hat{\boldsymbol{\eta}}) = (\boldsymbol{B}\boldsymbol{\eta} - \boldsymbol{B}\hat{\boldsymbol{\eta}}) \tag{7}$$

$$\dot{\boldsymbol{e}} = (\boldsymbol{B}\dot{\boldsymbol{\eta}} - \boldsymbol{B}\dot{\hat{\boldsymbol{\eta}}}) = (\boldsymbol{B}\boldsymbol{A}\boldsymbol{\eta} - \boldsymbol{B}\dot{\hat{\boldsymbol{\eta}}}) = (\boldsymbol{A}\boldsymbol{y} - \boldsymbol{B}\dot{\hat{\boldsymbol{\eta}}}) \tag{8}$$

By substituting Eq. (6) into Eq. (8), it can be obtained

$$\dot{\boldsymbol{e}} = \left\{ \boldsymbol{A}(\boldsymbol{e} + \boldsymbol{B}\hat{\boldsymbol{\eta}}) - \boldsymbol{B}(\hat{\boldsymbol{A}}\hat{\boldsymbol{\eta}} + \boldsymbol{\alpha}(\boldsymbol{y} - \boldsymbol{B}\boldsymbol{\eta}) + \boldsymbol{\beta}\mathrm{sgn}(\boldsymbol{y} - \boldsymbol{B}\boldsymbol{\eta})) \right\} \tag{9}$$

After simplifying Eq. (9) into Eq. (10)

$$\dot{\boldsymbol{e}} = \left\{ \boldsymbol{B}(\boldsymbol{A} - \boldsymbol{\alpha}\boldsymbol{B})\boldsymbol{B}^{\mathrm{T}}\boldsymbol{e} - \boldsymbol{B}(\hat{\boldsymbol{A}} - \boldsymbol{A})\hat{\boldsymbol{\eta}} - \boldsymbol{B}\boldsymbol{\beta}\mathrm{sgn}(\boldsymbol{e}) \right\} \tag{10}$$

The error of the parameter estimation, $e_u = \hat{u} - u$, where $\hat{u}$ is the estimate of $u$ for the errors $e$ and $e_u$. The Lyapunov function is considered as follows

$$U(e, e_u) = e^{\mathrm{T}}e + \frac{e_u^2}{\mu} \qquad \lambda > 0 \tag{11}$$

$$\dot{U}(e, e_u) = e^{\mathrm{T}}\dot{e} + \dot{e}^{\mathrm{T}}e + \frac{2e_u}{\mu}\dot{\hat{v}} \tag{12}$$

Substituting Eq. (10) into Eq. (12)

$$\dot{U}(e, e_u) = p_1 + p_2 \tag{13}$$

$$p_1 = \boldsymbol{e}^{\mathrm{T}} \left\{ \left[ \boldsymbol{B}(\boldsymbol{A} - \boldsymbol{\alpha}\boldsymbol{B})\boldsymbol{B}^{\mathrm{T}} \right]^{\mathrm{T}} + \left[ \boldsymbol{B}(\boldsymbol{A} - \alpha\boldsymbol{B})\boldsymbol{B}^{\mathrm{T}} \right] \right\} \boldsymbol{e} - \boldsymbol{\beta}^{\mathrm{T}}\boldsymbol{B}^{\mathrm{T}}\boldsymbol{e}\mathrm{sgn}(\boldsymbol{e}) - \boldsymbol{e}^{\mathrm{T}}\boldsymbol{B}\boldsymbol{\beta}\mathrm{sgn}(e)$$

$$p_2 = \frac{2e_u}{\mu}\dot{\hat{u}} - \hat{\boldsymbol{\eta}}^{\mathrm{T}}(\hat{\boldsymbol{A}} - \boldsymbol{A})^{\mathrm{T}}\boldsymbol{B}^{\mathrm{T}}\boldsymbol{e} - \boldsymbol{e}^{\mathrm{T}}\boldsymbol{B}(\hat{\boldsymbol{A}} - \boldsymbol{A})\hat{\boldsymbol{\eta}}$$

Proper selection of $\alpha$ and $\beta$ is conducted in such a way that $\beta$>0 and $Re[\lambda(\boldsymbol{A} - \boldsymbol{\alpha}\boldsymbol{B})] < 0$, such that part-1 ($p_1$) of Eq. (13) would always be less than zero except at the origin [21]. Therefore, for the Lyapunov stability, part-2 ($p_2$) of Eq. (13) is zero.

$$\frac{2e_u}{\mu}\dot{\hat{u}} = \hat{\boldsymbol{\eta}}^{\mathrm{T}}(\hat{\boldsymbol{A}} - \boldsymbol{A})^{\mathrm{T}}\boldsymbol{B}^{\mathrm{T}}\boldsymbol{e} + \boldsymbol{e}^{\mathrm{T}}\boldsymbol{B}(\hat{\boldsymbol{A}} - \boldsymbol{A})\hat{\boldsymbol{\eta}} \tag{14}$$

By the property of matrix transpose, the right-hand-side of Eq. (14) becomes

$$\frac{2e_u}{\mu}\dot{\hat{u}} = 2\hat{\boldsymbol{\eta}}^{\mathrm{T}}(\hat{\boldsymbol{A}}-\boldsymbol{A})^{\mathrm{T}}\boldsymbol{B}^{\mathrm{T}}\boldsymbol{e} = 2\begin{bmatrix}\hat{\eta}_1 & \hat{\eta}_2\end{bmatrix}\times\begin{bmatrix}0 & -(\hat{u}-u)\omega_n^2\\ 0 & 0\end{bmatrix}\times\begin{bmatrix}\omega_n^2\\ \omega_n\end{bmatrix}\times\boldsymbol{e} = -2\eta_1\omega_n^3 e_u e \tag{15}$$

$$\dot{\hat{u}} = -\mu\omega_n^3 e\times\hat{\eta}_1 \tag{16}$$

where Eq. (16) is the updated law for the estimation parameter $\hat{u}$, for which Eq. (13) is negative (i.e. $\dot{U}(e,e_u)<0$). Thus, it is stable according to the Lyapunov stability criteria.

Using $\hat{u}$ and $\hat{\eta}$, the state vector $\boldsymbol{v}$ and phase angle $\varphi$ of the input signal can be estimated as follows

$$\begin{bmatrix}\hat{v}_1\\ \hat{v}_2\end{bmatrix} = \boldsymbol{R}^{-1}\times\begin{bmatrix}\hat{\eta}_1\\ \hat{\eta}_2\end{bmatrix} = \begin{bmatrix}\omega_n^2 & \omega_n\\ -\hat{u}\omega_n^3 & \omega_n^2\end{bmatrix}\times\begin{bmatrix}\hat{\eta}_1\\ \hat{\eta}_2\end{bmatrix} \tag{17}$$

$$\hat{\varphi} = \mathrm{atan2}\left(\frac{\hat{\omega}\hat{v}_1}{\hat{v}_2}\right) \tag{18}$$

After integrating Eq. (17), the fundamental component of the input signal ($v_{sfa}$) can be computed as

$$v_{sfa} = \hat{v}_1 = \omega_n^2\times\hat{\eta}_1 + \omega_n^2\times\hat{\eta}_1 \tag{19}$$

Similarly, the fundamental components of the remaining phases "b" and "c" are ($v_{sfb}$) and ($v_{sfc}$), respectively; they can also be computed, and will be utilized in reference voltage generation.

### 3.2 Load voltage amplitude and unit template generation

As part of the control of the DVR, the amplitude ($v_{LA}$) of the three-phase load voltage ($v_L$) for maintaining the terminal voltage at its level is generated using regulators. It is also necessary to compute the unit templates that have to be used in the generation of the loss component ($v_p$) and voltage regulation component ($v_q$) of the DVR reference load voltage. Therefore, the sensed load voltage is processed through Eq. (20) to obtain its amplitude as [4]

$$V_{LA} = \sqrt{2/3\times(v_{La}^2+v_{Lb}^2+v_{Lc}^2)} \tag{20}$$

The in-phase templates ($x_p$) and quadrature templates ($x_q$) are computed using Eq. (21) after determining the amplitude of the load current ($I_{LA}$) from three-phase load currents ($i_L$), as follows [4]

$$\begin{cases} x_{pa} = \dfrac{i_{La}}{I_{LA}} & x_{pb} = \dfrac{i_{Lb}}{I_{LA}} & x_{pc} = \dfrac{i_{Lc}}{I_{LA}} \\ x_{qa} = \dfrac{x_{pc}-x_{pb}}{\sqrt{3}} & x_{qb} = \dfrac{3x_{pc}+x_{pb}-x_{pc}}{2\sqrt{3}} & \\ x_{qc} = \dfrac{-3x_{pc}+x_{pb}-x_{pc}}{2\sqrt{3}} & & \end{cases} \tag{21}$$

### 3.3 Reference load voltage and PWM gate pulse generation

Using the three-phase fundamental components of supply voltage ($v_{sf}$), loss components ($v_p$) computed using Eq. (22), and voltage regulation components ($v_q$) computed using Eq. (23), the three-phase load reference voltages ($v_L^*$) can be generated using Eq. (24). Finally, the three-phase reference load voltages ($v_L^*$) are compared with the actual three-phase load voltage ($v_L$). The errors obtained are again processed through a carrier-based triangular wave of 5 kHz to generate PWM pulses for three single-phase VSCs that function as a DVR.

$$v_{pa} = V_{DPI}\times x_{pa} \quad v_{pb} = V_{DPI}\times x_{pb} \quad v_{pc} = V_{DPI}\times x_{pc} \tag{22}$$

$$v_{qa} = V_{LPI}\times x_{qa} \quad v_{qb} = V_{LPI}\times x_{qb} \quad v_{qc} = V_{LPI}\times x_{qc} \tag{23}$$

$$v_{Labc}^* = v_{sfabc} - v_{pabc} + v_{qabc} \tag{24}$$

### 3.4 Optimization approach for PI controller tuning

PI controllers have become a part of most control algorithms, for which an optimization approach has been adapted for tuning the PI gains. Optimization methods are indirectly treated as approximate methods that can be classified with respect to their nature of inspiration. The MFO algorithm, which is a nature-inspired optimization algorithm, has been implemented for tuning PI controllers used in the SMAO-based control algorithm [24]. The basic required parameters for the MFO algorithm to be implemented are listed as Eqs. (25)-(27) [24]

$$a = -\left(1+\frac{i_p}{i_m}\right) \tag{25}$$

$$F_n = round\left(N - \frac{i_p\times(N-1)}{i_m}\right) \tag{26}$$

$$T = (a-1)\times rand() + 1 \tag{27}$$

where $F_n$ is the Flame number, $N$ is the maximum count of flames, $i_p$ is the present iteration, and $i_m$ maximum iterations are considered.

The cost function defined for PI controller gain tuning while reducing error $e$ between reference quantity and actual quantity toward zero is shown in Eq. (28). This cost function is derived from one of the performance indexes, integral time squared error (ITSE), with the simulation time $t$. The objective function is the combination of integral time squared error-1 (ITSE-1) and ITSE-2. Here, it is understood that ITSE-1 is the objective function for the DC-PI controller, whereas ITSE-2 is the objective function for the AC-PI controller. In this study, both objective functions are given the same importance. Thus, the combined objective function is modeled as $F_{obj}$=(0.5×ITSE-1)+(0.5×ITSE-2). Here, 0.5 indicates that 50% weightage has been given to both PI controllers.

$$Cost\ function = \int t \times e^2 \mathrm{d}t \tag{28}$$

Eq. (29) and Eq. (30) are the distance and position updating equations of the MFO algorithm, on which the entire optimization depends [24].

$$\begin{cases} D = \mathrm{abs}\left(F\_pos_{i_p,d} - M\_pos_{i_p,d}\right) \\ M\_pos_{i_p,d} = D * e^{b.T} * \cos\left(2\pi \times T\right) + F\_pos_{i_p,d} \end{cases} \quad M\_pos \leqslant F_n \tag{29}$$

$$\begin{cases} D = \mathrm{abs}\left(F\_pos_{i_p,d} - M\_pos_{i_p,d}\right) \\ M\_pos_{i_p,d} = D * e^{b.T} * \cos\left(2\pi \times T\right) + F\_pos_{F_n,d} \end{cases} \quad M\_pos > F_n \tag{30}$$

where $D$ is the distance between the moths, $d$ is the dimension of the moth, $F\_pos$ is the sorted moth position, and $M\_pos$ is the position of the present moth. However, some of the parameters are initially considered for the implementation of the MFO optimization algorithm. The study of optimized PI controller gain tuning is presented with the help of a convergence curve, and figures showing the change in values of the PI controller gains ("$k_p$" and "$k_i$") with respect to each iteration are shown in Fig. 3. Fig. 3a shows the variation in the cost function value, as defined in Eq. (28), with respect to iterations. From the cost function variation, it can be seen that the variation in the cost function values is very small at steps of 0.01, which shows that the cost function almost converges. After many tests, for a maximum of 10 iterations, from iteration number 8 onward, the cost function is stabilized. This shows that the variation of the PI gains is settled by the 8th iteration, which can be seen in Fig. 3b and Fig. 3c, respectively, for the DC-PI controller and AC-PI controller. The variation in "$k_p$" and "$k_i$" in the DC-PI controller with each iteration is taken on the left and right $y$-axis of the same plot with iterations on the $x$-axis, as shown in Fig. 3b. Similarly, for the AC-PI controller, Fig. 3b presents the variation in "$k_p$" and "$k_i$" in the AC-PI controller with each iteration taken on the left and right $y$-axis of the same plot with iterations on the $x$-axis. Therefore, after the complete optimization process of the PI controller gains by the MFO algorithm, the optimal value of the cost function is found to be 28.545. However, the tuned values of the DC-PI controller gains, "$k_p$" and "$k_i$" are 15.963 and 3.124, respectively. The tuned values of the AC-PI controller gains "$k_p$" and "$k_i$" are found to be 26.52 and 0.143, respectively. With these gains, SMAO controllers have been implemented for controlling 12-switch VSC-based DVR systems for various disturbance compensations.

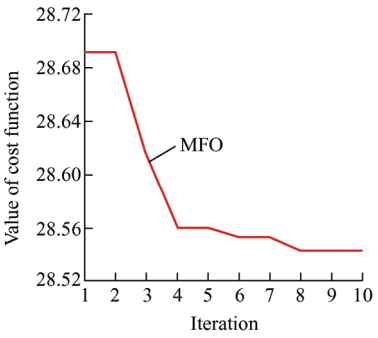


(a) Convergence curve of cost function

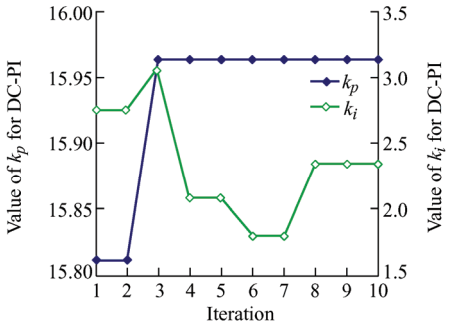


(b) Variation in value of DC-PI controller gain

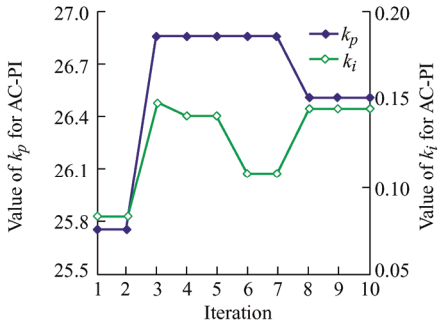


(c) Variation in value of AC-PI controller gain

Fig. 3 Change in values of the PI controller gains with respect to each iteration

## 4 Simulation study

The model of three single-phase VSC-based three-phase DVR systems was built and simulated in a Matlab software simulator. The Ode 4 solver was considered for the simulation configuration parameters with a sampling time of 10 μs. A DVR simulation study was conducted with a voltage sag, swell, imbalance, and phase shift in the supply voltage. Internal signals of the proposed control were provided to observe the effectiveness of the SMAO-based control algorithm. The evaluation of the DVR with SMAO control was performed for four different disturbances. The switching frequency of the PWM pulse generator was considered to be 5 kHz. The DVR system parameters for the implementation work are given in Appendix-A.

### 4.1 DVR reference load voltage generation using SMAO control

For control algorithm evaluation, supply voltages with different voltage-based power quality problems were considered, and the performances are shown in Fig. 4. In this figure, subplots (1, 6) show internal signals of the SMAO-estimating fundamental component ($v_{sfa}$) of phase "a" from input supply voltage ($v_{sa}$) of phase "a". Internal signals ($\eta_1$, $\eta_2$, and $u$) computed using Eq. (6) and Eq. (16) are presented in subplots (2-4) respectively, in Fig. 4. The phase angle error ($\Phi_e$) between the estimated phase angle ($\Phi$) and actual phase angle is shown in subplot (5). Subplot (6) of Fig. 4 depicts the fundamental component ($v_{sfa}$) of phase "a" computed using Eq. (19). Similarly, the fundamental components ($v_{sf}$) of the three-phase supply voltage have been computed and shown in subplot (7) of Fig. 4, which must be further used in the load reference voltage generation. Subplots (8) and (9) of Fig. 4 provide information on the outputs of the DC-PI controller and AC-PI controller, respectively. In-phase ($x_p$) and quadrature ($x_q$) unit templates generated using Eq. (21) are shown in subplots (10) and (11) of Fig. 4, respectively. The loss component ($v_p$) and voltage regulation component ($v_q$) are computed using Eq. (22) and Eq. (23). These are represented in subplots (12) and (13), respectively, of Fig. 4. The three-phase load reference voltage ($v_L^*$) generated using Eq. (24) is shown in subplot (14) of Fig. 4. The actual three-phase load voltage ($v_L$) was pictorially compared with the load reference voltage ($v_L^*$), as shown in Fig. 4. The actual load voltage ($v_L$) and load reference voltage ($v_L^*$) generated were compared, and the resultant errors were processed using a PWM pulse generator, which gave pulses to the 12-switch VSC.

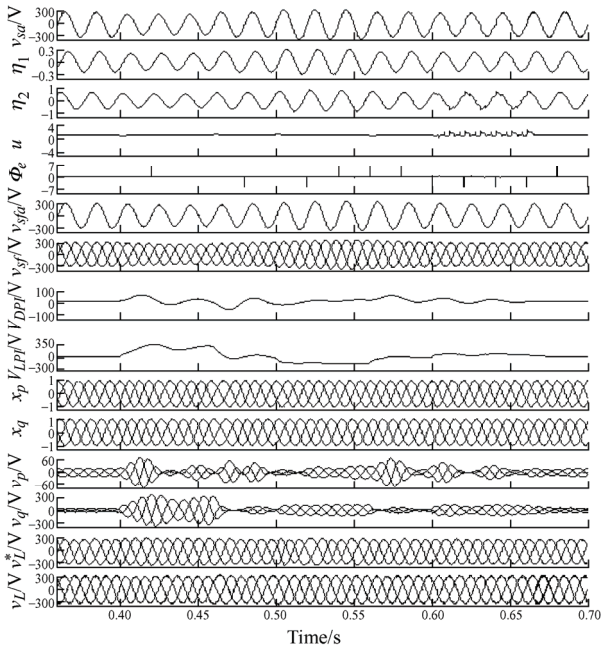


Fig. 4 Internal signals of SMAO control algorithm showing generation of reference load voltage

### 4.2 Compensation of different disturbances in supply voltage using DVR

This section discusses the dynamic performance of the DVR to compensate for the different disturbances imposed on the supply voltage. Fig. 5 shows the capability of the DVR when the supply voltage is affected by four different disturbances. Fig. 5a

represents the compensation of the voltage sag, swell, and disturbances in the supply voltage. Fig. 5b shows the compensation of the phase jump in the supply voltage, in which a 30° phase jump (lagging) was created in the supply voltage. In Fig. 5a, subplot (1) is the three-phase supply voltage ($v_s$) with sag, swell, and distortions in three cycles of 60 ms each with two cycles (40 ms) of normal supply between each disturbance. The compensated voltages ($v_c$) are shown in subplots (2-4) of Fig. 5a for the three phases for clear observation.

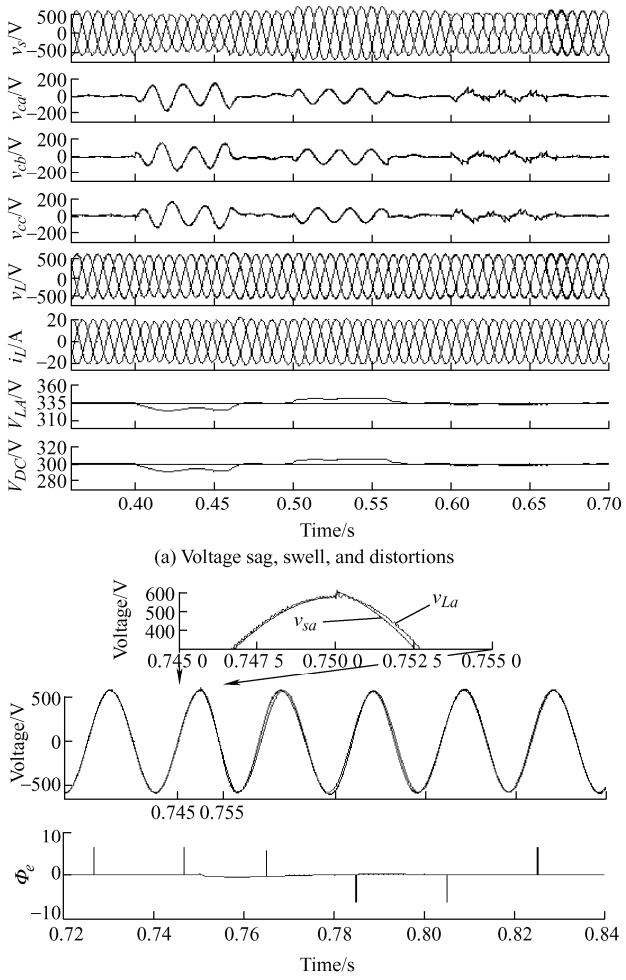


(a) Voltage sag, swell, and distortions




(b) Phase angle jump

Fig. 5 DVR performance in compensation and distortions

The three-phase load voltage ($v_L$) after compensation of disturbances is shown in subplot (5) of Fig. 5a. Subplot (6) of this figure shows the three-phase load current ($i_L$), which is also similar to the supply current ($i_s$), as DVR is a series-connected compensation device. The load voltage amplitude ($V_{LA}$) and DC-link voltage ($V_{DC}$) were maintained near their references, as shown in subplots (7-8) of Fig. 5a.

The phase jump compensation is presented in Fig. 5b, in which both the supply voltage ($v_{sa}$) and load voltage ($v_{La}$) of phase "a" are shown. A phase jump of 30° (lagging) was created at a supply voltage of 0.75 s, as shown in subplot (2) of Fig. 5b. The magnified portion of the phase jump in the supply voltage is clearly seen in subplot (1) of Fig. 5b. It is understood that a phase jump in the supply voltage ($v_{sa}$) is not observed in the load voltage ($v_{La}$) within one cycle. Subplot (3) of Fig. 5b shows the error ($\Phi_e$) between the estimated phase angle ($\varphi$) and the actual phase angle. It is observed that the phase-jump compensation using the DVR is within one cycle.

### 4.3 DVR performance in steady state with SMAO control

Fig. 6 depicts the performance of the DVR in the steady state, which is analyzed during harmonics included in the supply voltage ($v_s$). In this figure, the supply voltage ($v_{sa}$), load voltage ($v_{La}$), and load current ($i_{La}$) of the phase are considered for the steady-state analysis. The total harmonic distortions (THDs) of these three waveforms were observed and are shown in Figs. 6a-6c.

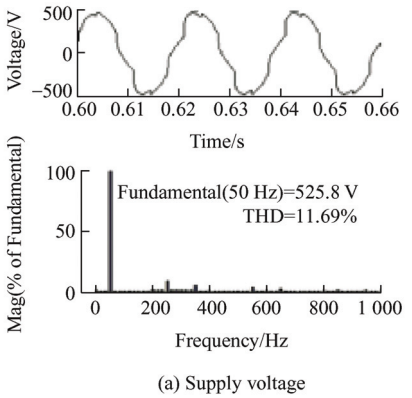


(a) Supply voltage

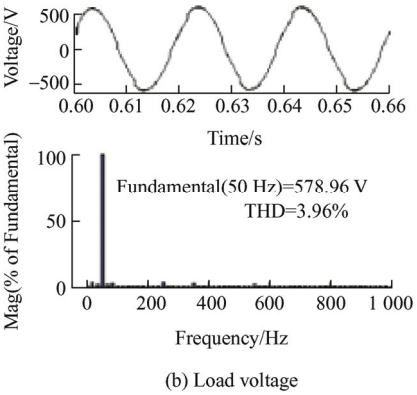


(b) Load voltage

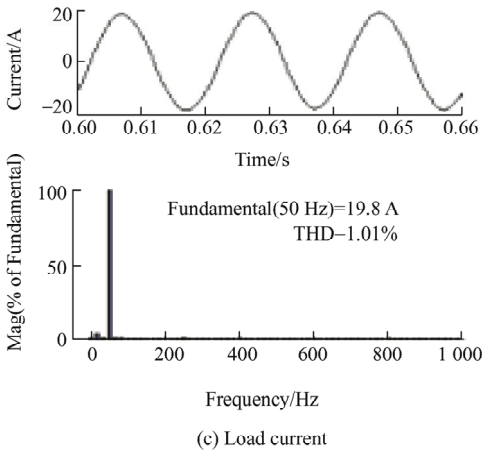


(c) Load current

Fig. 6 Total harmonic distortions (THDs) of three waveforms

A supply voltage with distortions of 11.69% THD with a 525.8 V fundamental voltage can be seen in Fig. 6a. After compensation of distortions, the load voltage can be found to be distortion-free with 3.96% of the THD having a fundamental voltage of 578.96 V, as presented in Fig. 6b. Because the sensitive load considered is linear, and the load current has no effect on voltage distortions, it has negligible waveform distortion in terms of the THD of 1.01% with 19.8 A. It has been found that the required quality of the voltage after compensation is under the limit of IEEE standards [25].

## 5 Experimental results

Three units of single-phase VSC-based DVR systems were developed for performance testing of the control algorithm in a laboratory environment, as shown in Fig. 7. The SMAO-based control for the DVR was tested with different disturbances in supply voltage on a real-time processor using a Micro Lab Box (RTI1202) Xilinx® Kintex®-7 XC7K325T programmable FPGA real-time simulator. The Micro Lab Box (RTI1202) is a real-time processor made using d-SPACE. The sampling time considered throughout the performance was 40 μs. The control algorithm was evaluated by observing the internal signals when sag and distortions were included in the supply voltage, as shown in Fig. 8 and Fig. 9, respectively.

However, Figs. 10-13 show the compensation capability of the DVR once the supply voltage is affected by sag, swell, distortions, and imbalance. The steady-state performance of the DVR was evaluated and recorded using a power quality analyzer (FLUKE-43B), as shown in Fig. 14. A four-channel digital signal oscilloscope (DSO) was used to capture the results during dynamic performance. Keysight/Agilent differential probes were used for the measurement of voltage. The parameters used for the DVR system are provided in Appendix-B.

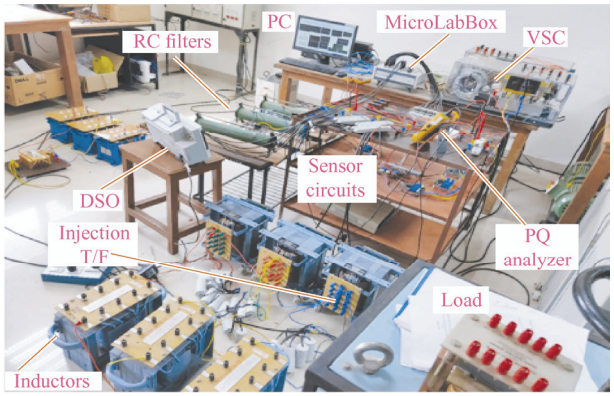


Fig. 7 Laboratory setup of 6-leg VSC based DVR

### 5.1 Performance of sliding mode adaptive observer

The extraction of reference load voltage through an AO-based control algorithm is demonstrated for phase "a" in the case of sag and distortions in Fig. 8 and Fig. 9 respectively. Figs. 8a-8f show the internal signals, such as fundamental positive sequence components (FPSC), and unit templates, including supply voltage with sag in it. Fig. 8a shows the supply voltage ($v_{sa}$) with sag, intermediate signals ($\eta_1$, $\eta_2$), and fundamental positive sequence of the supply voltage ($v_{sa1}$). Fig. 8b shows the supply voltage ($v_{sa}$) and fundamental positive sequence of the supply voltage ($v_{sa1}$) along with the ratio of the system frequency and nominal system angular frequency ($u$) and phase angle ($\theta$).

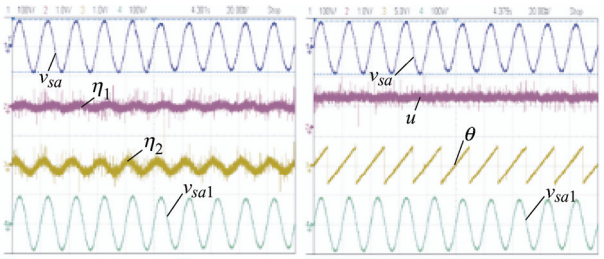


(a) In $y$-axis Ch1: 100 V/div, Ch2: 1 V/div, Ch3: 1 V/div, Ch4: 100 V/div and in $x$-axis 20 ms/div

(b) In $y$-axis Ch1: 100 V/div, Ch2: 1 V/div, Ch3: 5 V/div, Ch4: 100 V/div and in $x$-axis 20 ms/div

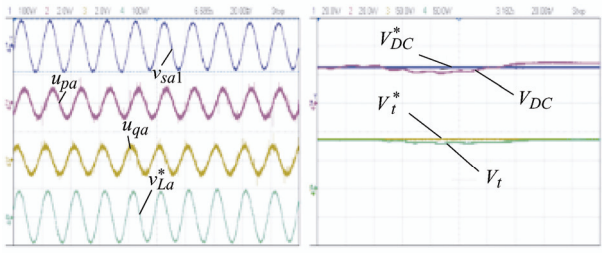


(c) In *y*-axis Ch1: 100 V/div, Ch2, 3: 2 V/div, Ch4:100 V/div and in *x*-axis 20 ms/div

(d) In *y*-axis Ch1, 2: 20 V/div, Ch3, 4: 50 V/div and in *x*-axis 20 ms/div

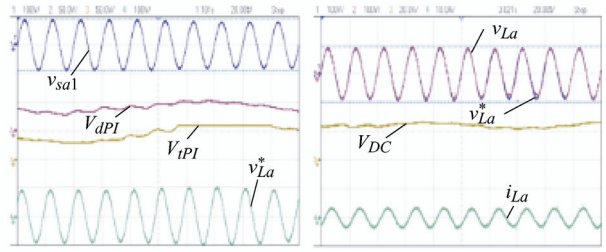


(e) In *y*-axis Ch1, 4: 100 V/div, Ch2, 3: 50 V/div and in *x*-axis 20 ms/div

(f) In *y*-axis Ch1, 2: 100 V/div, Ch3: 20 V/div, Ch4: 10 A/div and in *x*-axis 10 ms/div

Fig. 8 Internal signals of SMAO-based control algorithm in the case of sag in supply voltage

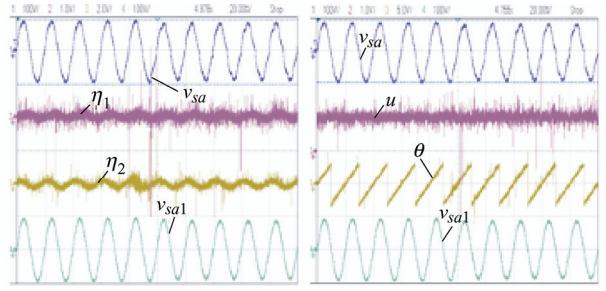


(a) In *y*-axis Ch1: 100 V/div, Ch2: 1 V/div, Ch3: 2 V/div, Ch4: 100 V/div and in *x*-axis 20 ms/div

(b) In *y*-axis Ch1: 100 V/div, Ch2: 1 V/div, Ch3: 5 V/div, Ch4: 100 V/div and in *x*-axis 20 ms/div

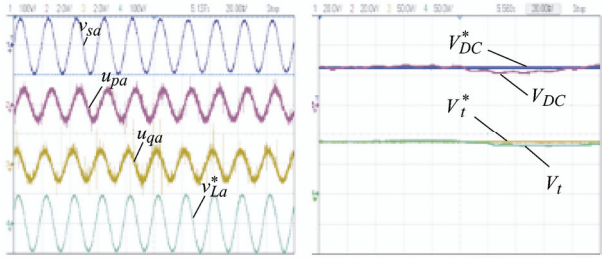


(c) In *y*-axis Ch1: 100 V/div, Ch2, 3: 2 V/div, Ch4:100 V/div and in *x*-axis 20 ms/div

(d) In *y*-axis Ch1, 2: 20 V/div, Ch3, 4: 50 V/div and in *x*-axis 20 ms/div

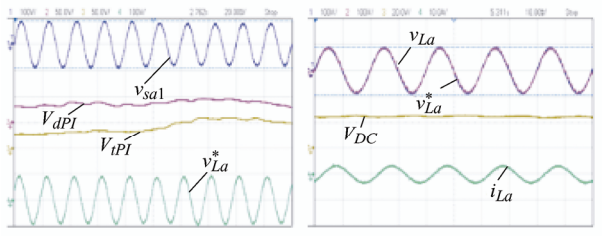


(e) In *y*-axis Ch1, 4: 100 V/div, Ch2, 3: 50 V/div and in *x*-axis 20 ms/div

(f) In *y*-axis Ch1, 2: 100 V/div, Ch3: 20 V/div, Ch4: 10 A/div and in *x*-axis 10 ms/div

Fig. 9 Internal signals of SMAO-based control algorithm in case of distortions in supply voltage

Fig. 8c shows the positive sequence components of the supply voltage ($v_{sa1}$) along with unit templates of phase "a", ($u_{pa}$) and ($u_{qa}$), and load reference voltage ($v^*_{La}$). Fig. 8d shows a comparison of the reference DC-link voltage ($V^*_{DC}$) with its actual ($V_{DC}$) and load voltage terminal value ($V^*_t$) with its actual value ($V_t$), and it can be seen that both the DC-link voltage and load terminal voltage are maintained at their reference values. The reference load voltage ($v^*_{La}$) with outputs of DC-PI and AC-PI controllers ($V_{dPI}$) and ($V_{tPI}$), along with the fundamental component of phase "a," ($v_{sa1}$), are shown in Fig. 8e. The load voltage tracking during the sag in supply voltage is depicted in Fig. 8f for phase "a" to show the success of the control algorithm. This figure shows the nature of the load reference voltage ($v^*_{La}$), actual load voltage ($v_{La}$), DC-link voltage ($V_{DC}$), and load current ($i_{La}$) during voltage variation.

Similarly, Figs. 9a-9f represent the same internal signals, but during the distortions in the supply voltage. The reference load voltage ($v^*_{La}$) generated here is further used to compare the actual load voltage ($v_{La}$) to obtain gate pulses to the VSC connected in a three-phase DVR system. Notably, the SMAO-based control algorithm generates the reference load voltage that is used to generate the gate pulses for three individual phases of VSCs.

### 5.2 Compensation of supply voltage disturbances using DVR

The dynamic voltage restorer was tested using the SMAO-based control algorithm to compensate for the different disturbances in the supply voltage. During the dynamics of the system, the test results were captured and are presented herein. In this section, the performance of DVR is discussed for the compensation of sag, swell, distortion, and system imbalance. Figs. 10-13 show the compensation of the voltage sag, swell, distortions, and unbalances, respectively, using the DVR with the SMAO-based control algorithm. The sag is created in supply voltage ($v_{sabc}$), as shown in Fig. 10a, and its corresponding load voltage ($v_{Labc}$) after compensation is set back to its desired value, that is, 110 V RMS, as shown in Fig. 10b. Fig. 10c shows the supply voltage ($v_{sa}$), compensating voltage ($v_{cc}$), load voltage ($v_{La}$), and

load current ($i_{La}$) of phase "a", giving a clear picture of the sag compensation. Fig. 10d shows the same signals along with the DC-link ($V_{DC}$) in place of the compensating voltage. Fig. 11 shows the compensation of the voltage swell in the supply voltage. The swell is created in supply voltage ($v_{sabc}$), as shown in Fig. 11a, and its corresponding load voltage ($v_{Labc}$) after compensation is set back to its desired value, that is, 110 V RMS, as shown in Fig. 11b. Fig. 11c shows the supply voltage ($v_{sa}$), compensating voltage ($v_{cc}$), load voltage ($v_{La}$), and load current ($i_{La}$) of phase "a", giving a clear picture of the swell compensation. Fig. 11d shows the same signals along with a DC-link ($V_{DC}$) in place of the compensating voltage. Fig. 12 shows the compensation of the voltage distortions in the supply voltage. Distortion levels of more than 8% were created in the supply voltage ($v_{sabc}$), as shown in Fig. 12a, and its corresponding load voltage ($v_{Labc}$) after compensation was set back to its desired value of 110 V RMS, as shown in Fig. 12b. Fig. 12c shows the supply voltage ($v_{sa}$), compensating voltage ($v_{cc}$), load voltage ($v_{La}$), and load current ($i_{La}$) of phase "a", giving a clear picture of the distortions compensation.

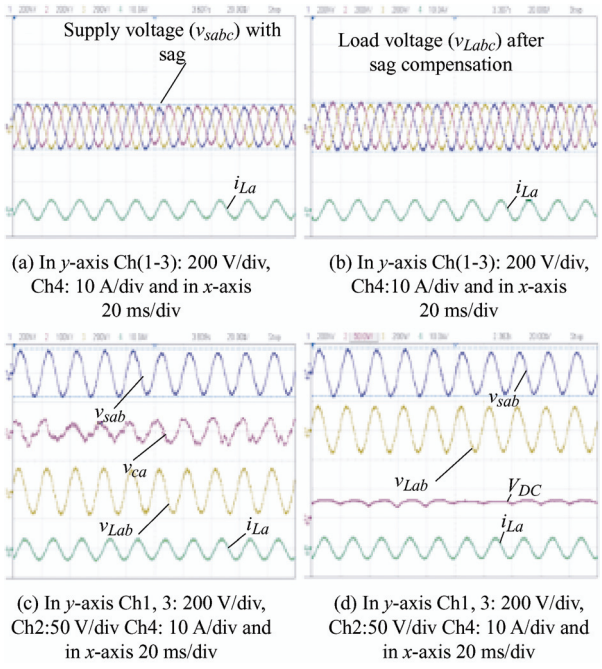


(a) In *y*-axis Ch(1-3): 200 V/div, Ch4: 10 A/div and in *x*-axis 20 ms/div

(b) In *y*-axis Ch(1-3): 200 V/div, Ch4:10 A/div and in *x*-axis 20 ms/div

(c) In *y*-axis Ch1, 3: 200 V/div, Ch2:50 V/div Ch4: 10 A/div and in *x*-axis 20 ms/div

(d) In *y*-axis Ch1, 3: 200 V/div, Ch2:50 V/div Ch4: 10 A/div and in *x*-axis 20 ms/div

Fig. 10 Performance of DVR in compensation of voltage Sag using SMAO-based control algorithm

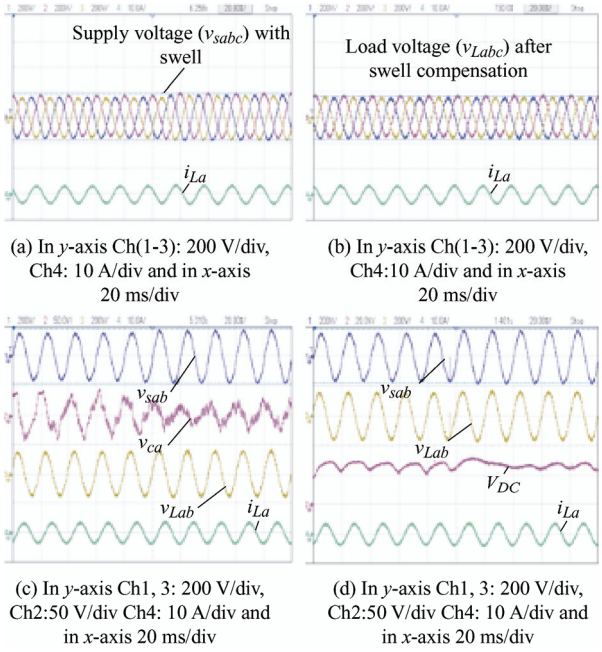


(a) In *y*-axis Ch(1-3): 200 V/div, Ch4: 10 A/div and in *x*-axis 20 ms/div

(b) In *y*-axis Ch(1-3): 200 V/div, Ch4:10 A/div and in *x*-axis 20 ms/div

(c) In *y*-axis Ch1, 3: 200 V/div, Ch2:50 V/div Ch4: 10 A/div and in *x*-axis 20 ms/div

(d) In *y*-axis Ch1, 3: 200 V/div, Ch2:50 V/div Ch4: 10 A/div and in *x*-axis 20 ms/div

Fig. 11 Performance of DVR in compensation of voltage swell using SMAO-based control algorithm

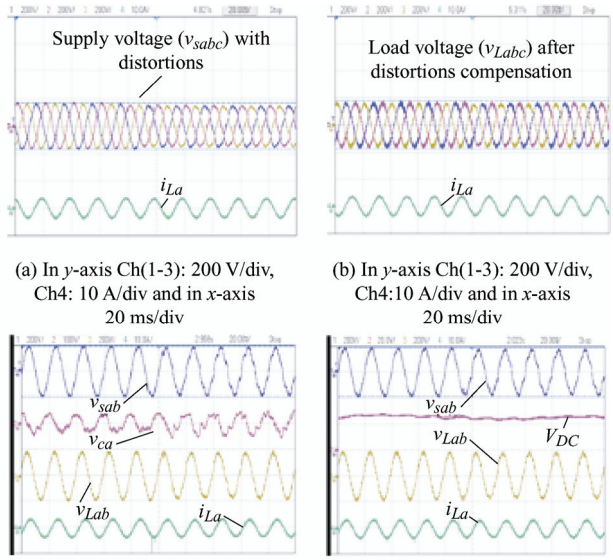


(a) In *y*-axis Ch(1-3): 200 V/div, Ch4: 10 A/div and in *x*-axis 20 ms/div

(b) In *y*-axis Ch(1-3): 200 V/div, Ch4:10 A/div and in *x*-axis 20 ms/div

(c) In *y*-axis Ch1, 3: 200 V/div, Ch2: 100 V/div Ch4: 10 A/div and in *x*-axis 20 ms/div

(d) In *y*-axis Ch1, 3: 200 V/div, Ch2: 20 V/div Ch4: 10 A/div and in *x*-axis 20 ms/div

Fig. 12 Performance of DVR in compensation of voltage distortions using SMAO-based control algorithm

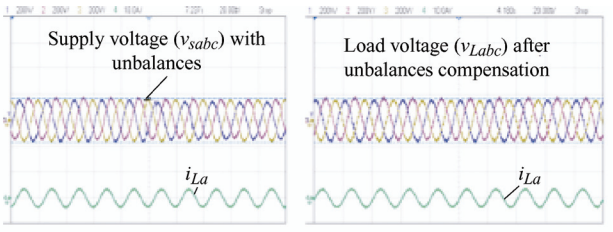


(a) In *y*-axis Ch(1-3): 200 V/div, Ch4: 10 A/div and in *x*-axis 20 ms/div

(b) In *y*-axis Ch(1-3): 200 V/div, Ch4: 10 A/div and in *x*-axis 20 ms/div

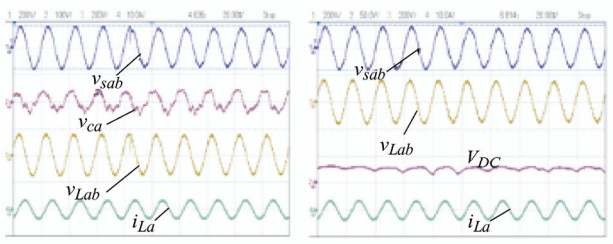


(c) In *y*-axis Ch1, 3: 200 V/div, Ch2: 50 V/div Ch4: 10 A/div and in *x*-axis 20 ms/div

(d) In *y*-axis Ch1, 3: 200 V/div, Ch2: 50 V/div Ch4: 10 A/div and in *x*-axis 20 ms/div

Fig. 13 Performance of DVR in compensation of voltage unbalances using SMAO-based control algorithm

Fig. 12d shows the same signals, along with the DC-link ($V_{DC}$), in place of compensating voltage for the verification of the DC-link voltage during the compensation. Fig. 13 shows the compensation of the voltage imbalance in the supply voltage. The supply voltage ($v_{sabc}$) with unbalances is shown in Fig. 13a, and its corresponding load voltage ($v_{Labc}$) after compensation is set back to its desired value, which is 110 V RMS without any imbalance, as shown in Fig. 13b. Fig. 13c shows the supply voltage ($v_{sa}$), compensating voltage ($v_{cc}$), load voltage ($v_{La}$), and load current ($i_{La}$) of phase "a", giving a clear picture of unbalanced compensation. Fig. 13d shows the same signals along with DC-link ($V_{DC}$) in place of compensating voltage, for the verification of the DC-link voltage during unbalanced compensation. After observing the recorded waveform, it was noted that the DC-link voltage ($V_{DC}$) was maintained at the reference level with an effective dynamic response.

### 5.3 Compensation of voltage distortions during steady state condition

The steady-state performance of the DVR during distortions in the supply voltage is shown in Fig. 14. Fig. 14a shows the three-phase supply voltage ($v_{sab}$) with distortions with respect to the load current ($i_{La}$). The total harmonic distortions (THD) measured for supply voltage is presented in Fig. 14b. Fig. 14c shows the three-phase load voltages ($v_{Lab}$) with the load current ($i_{La}$). The THDs, which were measured for three-phase load voltages, are presented in Fig. 14d. The steady-state performance of the DVR during distortions in the supply voltage is presented in Tab. 1. This presents the three-phase supply voltages ($v_{sab}$, $v_{sbc}$, $v_{sca}$) with distortions with respect to the load current ($i_{La}$).

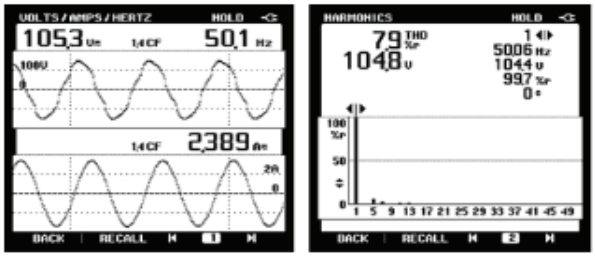


(a) Supply voltage ($v_{sab}$) and load current ($i_{La}$)

(b) THD of $v_{sab}$

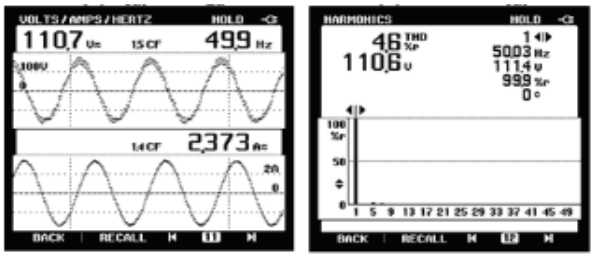


(c) Load voltage ($v_{Labc}$) and load current ($i_{La}$)

(d) THD of $v_{Lab}$

Fig. 14 Steady state performance of DVR using SMAO-based control algorithm during distortions in the supply voltage

The THDs that were measured for three supply voltages are also presented in Tab. 1. In Tab. 1, three-phase load voltages ($v_{Lab}$, $v_{Lbc}$, $v_{Lca}$) with load current ($i_{La}$), along with their THDs, can also be seen. Lastly, Tab. 1 gives the THD details of the load current of phase "a". From these results, it is clearly observed that the DVR can compensate the voltage distortion to maintain the load voltage at nominal voltage, and the harmonics levels are at the standard level of the IEEE: 519-2014 guidelines.

**Tab. 1 Experimental steady state results of DVR**

| Sr. No. | Quantity | During distortions (Voltage magnitude, % THD) |
|---|---|---|
| 1 | Supply voltage $v_{sab}$ | 105.3 V, 7.9 % |
| 2 | Supply voltage $v_{sbc}$ | 102.7 V, 8.1 % |
| 3 | Supply voltage $v_{sca}$ | 104.0 V, 8.0 % |
| 4 | Load voltage $v_{Lab}$ | 110.7 V, 4.6 % |
| 5 | Load voltage $v_{Lbc}$ | 110.9 V, 4.4 % |
| 6 | Load voltage $v_{Lca}$ | 110.4 V, 4.8 % |
| 7 | Load current $i_{La}$ | 2.396 A, 2.2 % |

## 6 Conclusions

A control based on the sliding mode AO is proposed to generate the reference load voltage for DVR from the estimated fundamental components of the supply voltage. The proposed control algorithm was tested on a three-phase dynamic voltage restorer and investigated for supply voltage sag, swell, phase jump, and voltage distortions. A self-supported three-phase VSC-based three-phase DVR was considered, which reduced the capacitor rating in comparison with the conventional three-leg VSC-based topology. An accurate estimation of the phase angle, system frequency, and fundamental component of the disturbed input voltage signal are the added features of the proposed control algorithm because of the consideration of frequency adaption. It was observed that the MFO algorithm provided the PI controller gains within eight iterations. From the simulation and experimental observations, it is clear that the DVR with the proposed control algorithm compensates for voltage-based power quality problems, such as sag, swell, and phase angle jump. The phase shift created in the supply voltage is compensated within one cycle of time. The load voltage distortions are reduced from the supply voltage, according to the levels of IEEE Std. 519-2014.

**Appendix-A System parameters for software work**

| Parameter | | Value |
|---|---|---|
| AC grid | Nominal voltage/V | 410 V(L-L), 50 Hz |
| | Load capacity | 10 kVA, 0.8 p.f. (lagg.) |
| DC-link capacitor $C_{DC}$/μF | | 1 200 |
| Interfacing inductors $L_i$/mH | | 1 |
| Filter parameters | $R_f$/Ω | 2 |
| | $C_f$/μF | 30 |
| Injection transformer | | 3 kVA (each transformer), 200/200 V |
| Sampling time $t_s$/μs | | 20 |
| Switching frequency $f_{sw}$/kHz | | 5 |
| SMAO parameters | $\mu$ | 0.008 |
| | $l_1$ | 0.000 1 |
| | $l_2$ | 40 |
| | $k_1$ | $0.01\times l_1$ |
| | $k_2$ | $0.01\times l_2$ |

**Appendix-B System parameters for experimental work**

| Parameter | | Value |
|---|---|---|
| AC grid | Nominal voltage/V | 110 V(L-L), 50 Hz |
| | Load capacity | 2.2 kVA, 0.8 p.f. (lagg.) |
| DC-link capacitor $C_{DC}$/μF | | 1 200 |
| Interfacing inductors $L_i$/mH | | 1.4 |
| Filter parameters | $R_f$/Ω | 2 |
| | $C_f$/μF | 60 |
| Injection transformer | | 1 kVA (each transformer), 100/100 V |
| Sampling time $t_s$/μs | | 40 |
| Switching frequency $f_{sw}$/kHz | | 5 |
| SMAO parameters | $\mu$ | 0.008 |
| | $l_1$ | 0.000 1 |
| | $l_2$ | 40 |
| | $k_1$ | $0.01\times l_1$ |
| | $k_2$ | $0.01\times l_2$ |

## References


[1] M P Kazmierkowski, R Krishnan, F Blaabjerg. Control in power electronics: Selected problems. New York: Elsevier Science, 2002.

[2] A Yazdani, R Iravani. Voltage-sourced converters in power systems: Modeling, control, and applications. Hoboken: John Wiley and Sons, 2010.

[3] R S Vedam, M S Sarma. Power quality: VAR compensation in power systems. New York: CRC Press, 2008.

[4] B Singh, A Chandra, K Al-Haddad. Power quality: Problems and mitigation techniques. London: John Wiley and Sons, 2014.

[5] D Patel, A K Goswami, S K Singh. Voltage sag mitigation in an Indian distribution system using dynamic voltage restorer. *International Journal of Electrical Power and Energy Systems*, 2015(71): 231-241.

[6] M Mansoor, N Mariun, A Toudeshki, et al. Innovating problem solving in power quality devices: A survey based on dynamic voltage restorer case (DVR). *Journal of Renewable and Sustainable Energy Reviews*, 2017(70): 1207-1216.

[7] A K Jindal, A Ghosh, A Joshi. Critical load bus voltage control using DVR under system frequency variation. *Journal of Electric Power Systems Research*, 2008, 78(2): 255-263.

[8] M H Haque. Voltage sag correction by dynamic voltage restorer with minimum power injection. *IEEE Power*

*Engineering Review*, 2001, 21(5): 56-58.

[9] F B Ajaei, S Afsharnia, A Kahrobaeian, et al. A fast and effective control scheme for the dynamic voltage restorer. *IEEE Trans. on Power Delivery*, 2011, 26(4): 2398-2406.

[10] G Nicolaescu, H Andrei, S Radulescu. Dynamic voltage restorer response analysis for voltage sags mitigation in MV networks with secondary distribution configuration. *Proc. IEEE 14th International Conference on Environment and Electrical Engineering*, 2014: 40-45.

[11] H Abdollahzadeh, M Jazaeri, A Tavighi. A new fast-converged estimation approach for dynamic voltage restorer (DVR) to compensate voltage sags in waveform distortion conditions. *International Journal of Electrical Power and Energy Systems*, 2014(54): 598-609.

[12] A E Leon, M F Farias, P E Battaiotto, et al. Control strategy of a DVR to improve stability in wind farms using squirrel-cage induction generators. *IEEE Trans. on power systems*, 2010, 26(3): 1609-1617.

[13] Peng Li, Lili Xie, Jiawei Han, et al. A new voltage compensation philosophy for dynamic voltage restorer to mitigate voltage sags using three-phase voltage ellipse parameters. *IEEE Trans. on Power Electronics*, 2017, 33(2): 1154-1166.

[14] A R A Jerin, P Kaliannan, U Subramaniam. Improved fault ride through capability of DFIG based wind turbines using synchronous reference frame control based dynamic voltage restorer. *ISA Transactions*, 2017(70): 465-474.

[15] N Kassarwani, J Ohri, A Singh. Performance analysis of dynamic voltage restorer using improved PSO technique. *International Journal of Electronics*, 2019, 106(2): 212-236.

[16] Guodong Chen, Liang Zhang, Ruiting Wang, et al. A novel SPLL and voltage sag detection based on LES filters and improved instantaneous symmetrical components method. *IEEE Trans. on Power Electronics*, 2015, 30(3): 1177-1188.

[17] E Ebrahimzadeh, S Farhangi, H I Eini, et al. Improved phasor estimation method for dynamic voltage restorer applications. *IEEE Transactions on Power Delivery*, 2015, 30(3): 1467-1477.

[18] D A Fernandes, F F Costa, J RS Martins, et al. Sensitive load voltage compensation performed by a suitable control method. *IEEE Transactions on Industry Applications*, 2017, 53(5): 4877-4885.

[19] S Biricik, H Komurcugil. Optimized sliding mode control to maximize existence region for single-phase dynamic voltage restorers. *IEEE Trans. on Industrial Informatics*, 2016, 12(4): 1486-1497.

[20] J J E Slotine, J K Hedrick, E A Misawa. On sliding observers for nonlinear systems. *Journal of Dynamic Systems, Measurement, and Control*, 1987, 109(3): 245-252.

[21] H Ahmed, S Amamra, I Salgado. Fast estimation of phase and frequency for single-phase grid signal. *IEEE Trans. on Industrial Electronics*, 2018, 66(8): 6408-6411.

[22] R Bansal, M Jain, B Bhushan. Designing of multi-objective simulated annealing algorithm tuned PID controller for a temperature control system. *Proc. 6th IEEE Power India International Conference (PIICON))*, 2014: 1-6.

[23] K Du, M N S Swamy. Search and optimization by metaheuristics. Montreal: Springer, 2016.

[24] O B Haddad. Advanced optimization by nature-inspired algorithms. Singapore: Springer, 2018.

[25] IEEE Recommended Practices and Requirement for Harmonic Control on Electric Power System. IEEE Std. 519-2014, 2014-06-11, doi: 10.1109/IEEESTD. 2014.6826459.

**Sabha Raj Arya** (M'12-SM'15) received Bachelor of Engineering degree in Electrical Engineering from Government Engineering College Jabalpur, in 2002, Master of Technology in Power Electronics from Motilal National Institute of Technology, Allahabad, in 2004 and Ph.D. degree in Electrical Engineering from Indian Institute of Technology (I.I.T) Delhi, New Delhi, India, in 2014. He joined as Assistant Professor, Department of Electrical Engineering, Sardar Vallabhbhai National Institute of Technology, Surat. In January 2019, he is promoted as Associate Professor in same institute. His fields of interest include power electronics, power quality, design of power filters and distributed power generation.

He received two national awards namely INAE Young Engineer Award from Indian National Academy of Engineering, POSOCO Power System Award from Power Grid Corporation of India in the year of 2014 for his research work. He is also received Amit Garg Memorial Research Award-2014 from I.I.T Delhi from the high impact publication in a quality journal during the session 2013-2014. At present, he has published more than hundred research papers in internal national journals and conferences in field of electrical power quality.

He also serves as an Associate Editor for the IET (UK) Renewable Power Generation.

**Rakesh Maurya** (M'16) received B.Tech. in Electrical Engineering from the Kamla Nehru Institute of Technology Sultanpur, Uttar Pradesh in 1998 and M.Tech. and Ph.D. in Electrical Engineering from Indian Institute of Technology Roorkee, India in 2002 and 2014 respectively. Presently, he is serving as Faculty Member in the Department of Electrical Engineering, Sardar Vallabhbhai National Institute of Technology Surat, Gujarat, India. His fields of interest include design of switching power converters, high power factor AC/DC converters, hybrid output converter, power quality problems, advanced electric drives and applications of real time simulator for the control of power converters.

**Talada Appala Naidu** (SM'18-M'20) received his B.Tech. in Electrical and Electronics Engineering from Jawaharlal Nehru Technical University, Kakinada, India, in 2012; and M.Tech. and Ph.D. in Electrical Engineering Department from Sardar Vallabhbhai National Institute of Technology, Surat, India, in 2016 and 2020 respectively. He has received Best Paper Award for one of his papers in IEEE conference PETPES-2019 at NIT Suratkal.

Dr. Naidu has worked as Visiting Researcher in Khalifa University of Science and Technology, Abu Dhabi after Ph.D. Later from Aug. 2020 to Aug. 2021, he worked as an Adhoc faculty in NIT, ANDHRA PRADESH. Currently he is with Dubai Electricity and Water Authority (DEWA) R&D Center, DEWA, Dubai, UAE. His fields of interest include applications of power electronics in distribution systems, power quality, renewable energy sources, smart grid integration, and artificial intelligence.

**Baladhandautham Chitti Babu** (SM'15) received the Ph.D. in Electrical Engineering from National Institute of Technology Rourkela, India in 2012. He had been with National Institute of Technology Rourkela, India as an Assistant Professor in Electrical Engineering Department from 2007 to 2013. Subsequently, he had two post-doc research appointments with Wroclaw University of Science & Technology, Poland from Dec. 2013 to June 2014 and VSB-Technical University of Ostrava, Czech Republic from Sep. 2014 to Sep. 2015. His research interests include power electronics applications in smart distribution grid containing renewable energy sources and low-power electronics design, including photovoltaic energy systems.